Materials Advances

ROYAL SOCIETY OF CHEMISTRY

PAPER

View Article Online
View Journal | View Issue

Cite this: *Mater. Adv.*, 2025, 6, 1719

Oxygen partial pressure effects on nickel oxide thin films and NiO/Si diode performance

Thi Kim Hang Pham,[a] Bao Quan Tran,[a] Khac Binh Nguyen,[b] Ngoc Yen Nhi Pham,[b] Thi Hai Yen Nguyen,[c] An Hoang-Thuy Nguyen,[d] Ngoc Phuong Nguyen,[e] Hai Dang Ngo*[a] and Hoai Phuong Pham*[b]

Received 7th November 2024,
Accepted 29th January 2025

DOI: 10.1039/d4ma01113a

rsc.li/materials-advances

In this work, nickel oxide thin films were grown on glass and n-type Si substrates using RF-magnetron sputtering in an oxygen-rich environment. The effects of elevated oxygen on the optical properties, electrical properties, ionic states, compositional analysis, surface morphology, and crystal structure are investigated. The X-ray diffraction data, which also demonstrate the presence of two phases in all samples: NiO and Ni_2O_3, indicate that the highly crystalline Ni_2O_3 phase in the nickel oxide thin film structure has a (002) growth orientation. According to X-ray photoelectron spectroscopy, the ratio of Ni^{3+} (Ni_2O_3 phase) to Ni^{2+} (NiO) states increases as the oxygen concentration increases. In the nickel oxide thin films, the ratio of Ni^{3+} states is substantially higher than that of Ni^{2+} states. The optical band gap is around 3.4 eV, as determined from UV-Vis transmission spectroscopy, and the average transmittance of nickel oxide thin films exceeds 50% in the visible spectrum. The nickel oxide thin films demonstrate a substantial carrier concentration between 2.33×10^{19} and 7.46×10^{19} cm^{-3}, with a minimum resistivity of 0.28 Ω cm. Furthermore, the p–n heterojunctions of the p-nickel oxide/n-silicon substrates revealed the optimal diode characteristic parameters at a 30% oxygen gas ratio. The results have been promising for further industrial development and fabrication of diodes.

1. Introduction

Nickel oxide (NiO) is an extensively explored material in the field of optoelectronics. p-type semiconducting NiO has a direct band gap energy ranging from 3.2 to 3.6 eV[1,2] It exhibits fair transmittance in the visible light region and strong electrical conductivity.[3,4] Furthermore, the exceptional chemical stability and eco-friendliness, as well as abundance of Ni make it a promising candidate for application in UV-photodetectors, transparent electrodes, and gas sensors.[5,6] In theory, stoichiometric NiO is an insulator with a high resistance of approximately 10^{13} Ω cm at room temperature.[7] Nevertheless, NiO is frequently chemically unbalanced because of two primary types of defects that result in good electrical conductivity: oxygen interstitials (O_i) and nickel vacancies (V_{Ni}).[8] The Ni vacancies were produced by providing an additional electron to oxygen during the ionization of two nearby Ni^{2+} ions into Ni^{3+}.[9] With a high amount of oxygen, chemical imbalance of nickel oxide thin films will lead to the appearance of additional oxidation states of nickel oxide, namely NiO_2 and Ni_2O_3. Hence, this exerts crucial impacts on different characteristics of NiO thin films.[10,11] Nandy *et al.* reported that the significant abundance of Ni^{3+} in the Ni_2O_3 compound has a strong influence in regulating the electrical characteristics of the NiO material, leading to the non-stoichiometric features of the nickel oxide thin film.[12] Furthermore, Ming-Chen Li *et al.* reported that the production of Ni^{3+} ions—which were regarded as color centers in accordance with the color center theory—often occurred concurrently with the generation of interstitial oxygen and nickel vacancies in nickel oxide thin films. As the concentration of Ni^{3+} grows, additional light-absorbing sites emerge, resulting in a reduction in the film's transmittance and the formation of a lackluster brown film. The additional oxygen atoms in the film absorb photons, which lowers the transmittance of the thin film.[13] K. Jouini *et al.* reported that gamma irradiation exceeding a dose of 5 kGy induced a phase transformation from NiO to Ni_2O_3, resulting in the formation of two NiO/Ni_2O_3 phases. This transformation reduced the band-gap value from

[a] *Faculty of Applied Sciences, Ho Chi Minh University of Technology and Education, 720700 Ho Chi Minh City, Vietnam. E-mail: dangnh@hcmute.edu.vn*
[b] *NTT Hi-Tech Institute, Nguyen Tat Thanh University, 298-300A Nguyen Tat Thanh Street, Ward 13, District 4, Ho Chi Minh City 700000, Vietnam. E-mail: phphuong@ntt.edu.vn*
[c] *Faculty of Science, Dong Nai University, 4 Le Quy Don Street, Tan Hiep Ward, Bien Hoa City 76111, Vietnam*
[d] *Department of Material Science and Engineering, Inha University, Incheon 111-12, Korea*
[e] *Institute of Applied Materials Science, Vietnam Academy of Science and Technology (VAST), 29TL Street, Thanh Loc Ward, District 12, Ho Chi Minh City 7000, Vietnam*

2.22 to 2.19 eV, corresponding to a new band at 431 nm in the absorption spectrum, at doses of 5 kGy and 10 kGy, thereby enhancing the photocatalytic activity compared to that of NiO.[10] However, a study regarding the properties of the films that simultaneously contain NiO and Ni_2O_3 phases is still missing.

In this report, reactive radio-frequency sputtering was implemented to generate nickel oxide films in an oxygen-rich environment. By using X-ray diffraction (XRD), scanning electron microscopy (SEM), X-ray photoelectron spectroscopy (XPS), UV-Vis transmission spectroscopy, and Hall effect measurements, the crystalline structure, surface morphology, the element composition, the optical qualities, and electrical properties were evaluated, respectively. In order to produce heterojunction diodes, p-type nickel oxide thin films were deposited on n-Si substrates, and their *I–V* characteristics were investigated.

2. Experiment

Nickel oxide thin films have been grown on glass and n-Si substrates *via* RF sputtering utilizing a nickel metallic target, using argon and oxygen as the working and reactive gases, respectively. The Si(001) substrate is prepared by cutting a Si (001) wafer (0.01–0.05 Ω cm, P-doped n-type, and single-side-polished) into a rectangular segment of area 1 inch × 1 inch. The Ni target exhibits a purity level of 99.95%. The ideal parameters for the deposition of NiO thin films are as follows: the deposition pressure is 5×10^{-3} Torr, with a constant RF power of 70 W. Nickel oxide thin films were deposited for one hour at 250 °C. The distance from the target to the sample holder is 7 cm. The argon to oxygen flow rate ratios are 8 : 2, 7.5 : 2.5, 7 : 3, and 6.5 : 3.5, corresponding to the samples N-20, N-25, N-30, and N-35, respectively. The glass substrates were first cleaned using acetone, ethanol, and isopropyl alcohol. The cleaning process for n-type Si substrates involves degreasing and etching to remove organic contaminants and native oxide coatings. The substrate is immersed in deionized (DI) water and 2-propanol for 40 seconds each in an ultrasonic bath. The Si substrate is submerged in 5% sulfuric acid (H_2SO_4) for 40 seconds and subsequently washed with 2-propanol for 40 seconds in an ultrasonic bath. Finally, it is etched for 30 seconds using dilute hydrofluoric acid (20% HF). The glass and Si substrates were preheated in a vacuum chamber at 150 °C and 325 °C for 15 minutes at a base pressure of 10^{-8} Torr. The In and Ni metals served as the contact channel for the diode.

The structural properties of nickel oxide thin films were analyzed using the X-ray diffraction technique (D8-ADVANCE). The thickness of nickel oxide was measured using a Talorstep profilometer (Rank-Taylor-Hobson, UK). By using a Talorstep profilometer, the thickness of the N-20 sample was measured to be 256 nm, that of the N-25 sample was 255 nm, that of the N-30 sample was 233 nm, and that of the N-35 sample was 222 nm.

The films' surface morphology was examined using a scanning electron microscope (SEM, S-4800 Hitachi). The optical characteristics of the nickel oxide thin films were investigated by UV-Vis spectroscopy (JASCO, V-550, Japan). The elemental composition of thin films was investigated by X-ray photoelectron spectroscopy (XPS) using Al Kα radiation on a Thermo Scientific X-ray photoelectron spectrometer. The electrical properties of NiO thin films were examined by Hall measurements (BIO-RAD HL5500IU). The current–voltage (*I–V*) characteristics at room temperature were studied using a Keysight U2722A current–voltage source. The junction area of the diode has a dimension of 0.5 cm × 0.5 cm.

3. Results and discussion

Fig. 1 shows the XRD patterns of nickel oxide thin films produced on glass and Si substrates at different oxygen flow rates. Nickel oxide deposited on glass surfaces displays a Ni_2O_3(002) peak [PDF#14-0481] and two peaks corresponding to NiO (111) and NiO (200) [PDF#47-1049], as seen in Fig. 1a.[14–16]

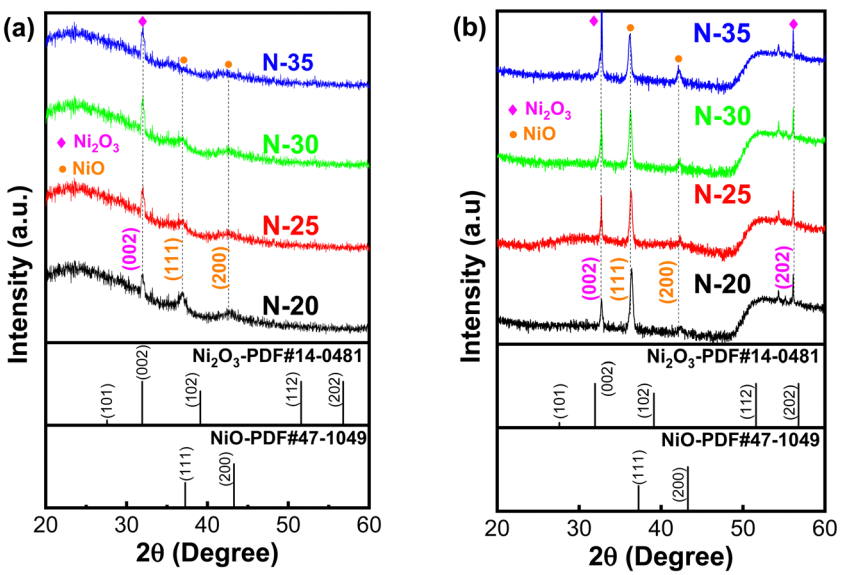

Fig. 1 X-ray diffraction (XRD) patterns of nickel oxide thin films at varying oxygen flow rates, grown on (a) glass substrate and (b) n-Si substrate.

Conversely, nickel oxide deposited on Si substrates displays similar peaks in addition to a Ni_2O_3 (202) peak (refer to Fig. 1b). In an oxygen-rich environment, nickel oxide thin films exist in both the Ni_2O_3 and NiO phases. The XRD results indicate significant differences in the phase composition of nickel oxide films that were deposited on glass compared to that of those deposited on Si substrates. On glass substrates, the Ni_2O_3 phase dominates, especially with increased oxygen flow rates (sample N-35). On Si substrates, the NiO phase exists at oxygen/argon ratios under 30%, whereas the Ni_2O_3 phase dominates at higher ratios.

The average crystallite size (D) of nanoscale materials can be calculated using Scherrer's equation.[17,18]

$$D = \frac{k\lambda}{\beta \cdot \cos(\theta)} \quad (1)$$

where λ represents the X-ray wavelength (λ = 0.15406 nm), β denotes the angular width of FWHM intensity observed at 2θ in radian, θ is Bragg's angle, and $k \approx 0.9$ is a constant (shape factor). The microstrain (ε) and dislocation density (δ) of the nickel oxide thin films were determined using the equations $\varepsilon = \frac{\beta}{4\tan(\theta)}$ and $\delta = \frac{1}{D^2}$, where D is the crystallite size which is regarded as one for minimum dislocation density.[17,18] The average crystallite sizes of the nickel oxide thin films grown on the glass substrate, derived from Scherrer equation, were 19.53 nm, 20.35 nm, 21.63 nm and 18.12 nm for N-20, N-25, N-30 and N-35, respectively. Evidently, as the partial oxygen ratio increases from 20% to 30%, the crystallinity of the nickel oxide thin film enhances. However, a further increase to 35% results in a decline of crystallinity. Conversely, an excessive oxygen amount will lead to the presence of numerous interstitial oxygen atoms in the film. Formation of defects induces diminished film crystallinity. This outcome is analogous to that reported in the previous work.

In addition, the structural mismatch between NiO (cubic structure) and Ni_2O_3 (hexagonal structure) results in the diffraction peak shifting to a higher angle, which in turn causes stacking faults to occur during the deposition process.[19,20] This result shows that in an oxygen-poor environment, the nickel oxide films are deposited with the stoichiometric nickel oxide (NiO) or the Ni^{2+} state predominates in the film structure. In contrast, in an oxygen-rich environment, the numerous Ni^{3+} ions generated in the nickel oxide crystal lattice will frequently combine with oxygen to form the Ni_2O_3 phase.[12] The creation of Ni^{3+} ions in the nickel oxide crystal lattice is ascribed to the charge displacement that occurs between two adjacent Ni^{2+} atoms, which is brought about by vacancies in the Ni atoms. The generation of Ni vacancies will contribute to increasing the concentration of hole carriers, thereby improving the conductivity of the nickel oxide thin film, which will be discussed in the electrical properties section. The structure parameters are shown in Table 1.

The surface morphology and grain sizes of nickel oxide thin films deposited on a glass substrate were analyzed using SEM and the line-cut method, as seen in Fig. 2. On the film surface,

Table 1 The XRD-derived characteristics of the (002) peak of nickel oxide/glass samples at varying oxygen percentages

Samples	2θ (°)	Full width at half maximum (FWHM) (°)	Crystallite size (nm)	Microstrain ($\times 10^{-3}$)	Dislocation density ($\times 10^{-3}$ nm^{-2})
N-20	31.97	0.42	19.53	6.44	2.62
N-25	31.99	0.41	20.35	6.18	2.42
N-30	32.01	0.38	21.63	5.87	2.14
N-35	32.01	0.46	18.12	6.94	3.05

the particles assume a relatively uniform shape. Despite the increase in the oxygen flow rate, the grain size (approximately 20 nm) and micro-strain were unaffected. Instead, it demonstrates a clearly stronger impact on the ratio of Ni^{3+} to Ni^{2+}. Consequently, the electrical and optical properties were also influenced, which will be discussed in sections to come. Moreover, as the flow of oxygen gas increases, the thickness of the nickel oxide film tends to decrease, probably as a result of the interaction between nickel and oxygen gas.[21,22] The outcome is oxidation and a growth of deficiencies within the nickel lattice, resulting in the formation of a NiOx lattice rather than an ideal NiO lattice.[23]

The elemental compositions and ionic states of nickel oxide films with different amounts of inlet oxygen were investigated using X-ray photoelectron spectroscopy (XPS), as shown in Fig. 3. The Ni $2p_{3/2}$ core in the energy range from 859 eV to 866 eV and the Ni $2p_{1/2}$ core in the energy range from 867 eV to 880 eV are represented by distinct spectral peaks in Fig. 3(a). Furthermore, the unique spectral peak of the core O 1s in the binding energy range from 527 to 533 eV can be observed in Fig. 3(b). The Ni $2p_{3/2}$ peak and the O 1s peak shift slightly to higher energy values when the oxygen content increases from 20% to 35%.[24] The peak shift of the Ni $2p_{3/2}$ and O 1s cores shows how the elevated oxygen ratio during the reactive sputtering process affects the constituents that make up the nickel oxide thin film. Moreover, a shift of about 0.5 eV of the O 1s core of the N35 sample compared with that of sample N20 is probably due to excessive oxygen in the N35 sample. They might absorb water on the surface and generate a small

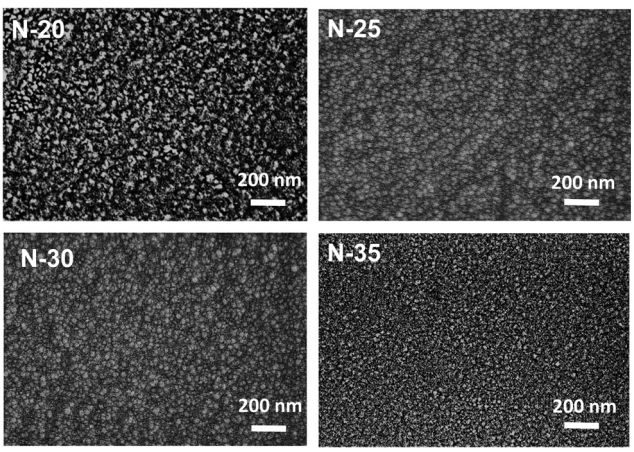

Fig. 2 SEM images of nickel oxide thin films deposited on the glass substrate with different oxygen flow rates.

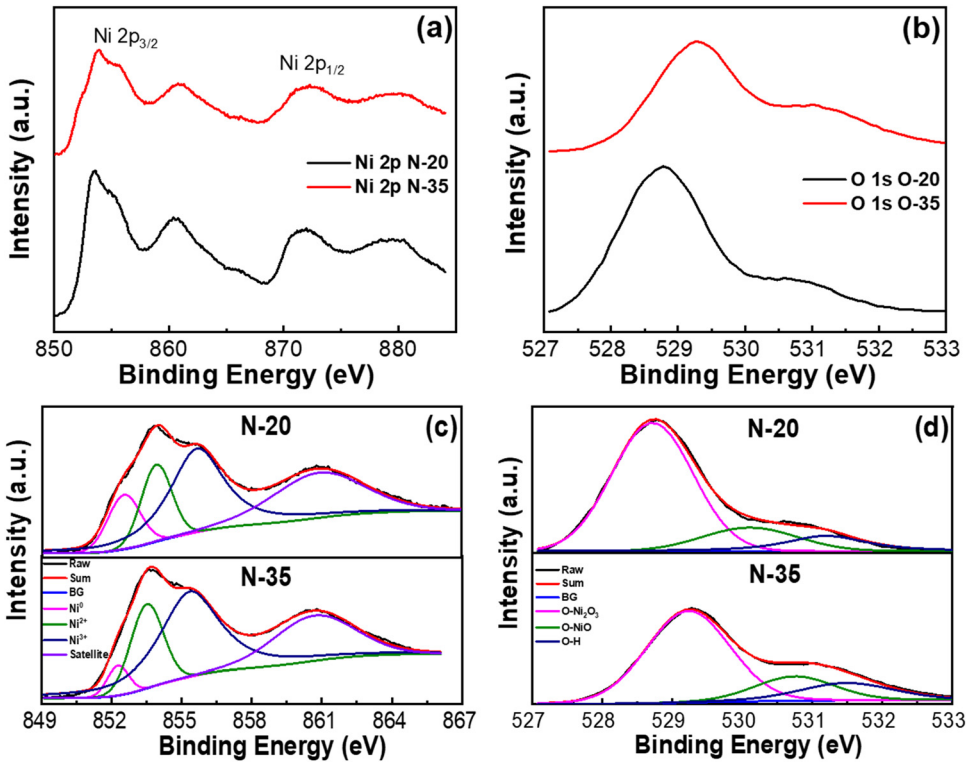

Fig. 3 (a) Ni 2p core level, (b) O1s core level, (c) deconvoluted Ni $2p_{3/2}$, and (d) deconvoluted O 1s spectra.

amount of NiOOH. The existence of NiOOH might cause a peak shift.[25]

Deconvoluting the Ni $2p_{3/2}$ core (Fig. 3(c)) and the O1s core (Fig. 3(d)) spectra will allow the focused examination of the ionic states contained in the nickel oxide thin film. There are peaks in the Ni $2p_{3/2}$ deconvolution spectrum around 855 eV, which suggest the presence of the Ni^{3+} state. Furthermore, the existence of the Ni_2O_3 phase is revealed in the reflected O1s spectrum by a peak at 529 eV. The O1s peak at 530 eV and the Ni $2p_{3/2}$ peaks, corresponding to the Ni^{2+} state, at 853 eV are for the nickel oxide (NiO) phase.[20,26,27] For all nickel oxide films, the Ni^0 peak is detected at 852 eV, whereas the satellite peaks are observed in the energy range of 861–862 eV (Ni $2p_{3/2}$).[28] Based on the area ratios of the Ni^{3+} peak (42.07%, 49.31%) and the Ni^{2+} peak (19.19%, 15.90%), the oxygen percentages are 20% and 35%. The area percentage of the Ni^{3+} peak increases from 42.07% to 49.31%, and the Ni^{2+} peak decreases from 19.19% to 15.90% as the oxygen percentage increases from 20% to 35%. As the amount of oxygen increases, so does the ratio of Ni^{3+} to Ni^{2+} states. The proportion of the Ni^{3+} state in all nickel oxide thin films is significantly higher than that of the Ni^{2+} state, which is consistent with previous research.[29]

In an oxygen-rich environment, a thin film of nickel oxide mainly occurs as Ni_2O_3. The Ni_2O_3 phase predominates, because of the presence of many Ni^{3+} cations, which form color centers and give the thin film a dark brown color.[26]

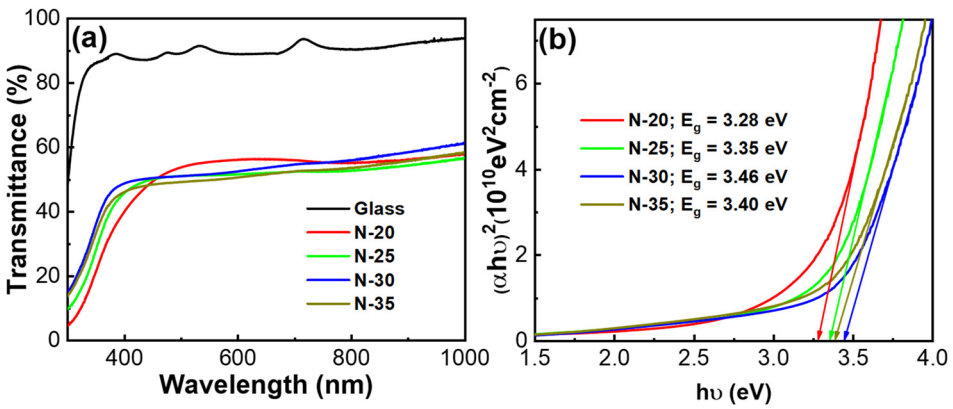

Fig. 4 Transmittance spectrum (a) and Tauc plot (b) of nickel oxide thin films deposited under different oxygen gas conditions.

The XPS results are consistent with the findings from the XRD analysis.

The transmittance of nickel oxide thin films grown under different oxygen flow conditions is demonstrated in Fig. 4. In the visible light spectrum, the relative average transmittance of the N-25, N-30, and N-35 samples is around 50% and tends to decrease as the percentage of oxygen increases. In addition, the absorption edge of the nickel oxide film presents a significant change. Specifically, when the oxygen ratio increases from 20 to 35%, the absorption edge shifts towards the short-wavelength region. The transmittance of the nickel oxide film in the UV region is comparatively high owing to the chemical balance of the film, with excess oxygen and hydrogen possibly existing in the form of –OH.[30] This result is consistent with earlier studies showing that being deposited in an oxygen-rich environment reduces the transparency of nickel oxide thin films.[31] The low transparency of the nickel oxide films in the visible light range is attributed to the existence of Ni^{3+} cations in the crystal lattice.[32] The second reason is that the transmittance of the thin film is lowered by the additional oxygen, which functions as scattering centers for incident light.

The bandgaps of nickel oxide thin films were determined from the Tauc plots: $h\nu = A(h\nu - E_g)^n$, which were derived from the absorption spectrum.[32] The relationship between the square of $(\alpha h\nu)$ and the photon energy $(h\nu)$ for crystalline nickel oxide thin films growing at various oxygen gas flow rates is illustrated in the inset of Fig. 4. It was found that nickel oxide thin films in an oxygen-excessive environment have optical bandgap energies of roughly 3.4 eV. Specifically, 3.28 eV, 3.35 eV, 3.46 eV, and 3.40 eV correspond to oxygen ratios of 20%, 25%, 30%, and 35%. Our nickel oxide thin films have a higher optical bandgap value than that of F. G. El Desouky.[33] This indicates that the optical bandgap is widened by the simultaneous presence of two phases, NiO and Ni_2O_3. Furthermore, higher oxygen ratios lead to higher carrier concentrations. Therefore, according to the Burstein–Moss effect, wider optical bandgaps come as a result of these degenerated semiconducting thin films.[34] However, if the oxygen ratio reaches above 35%, various defects will exist in the films. In addition, the defect density around grain boundaries is typically significantly greater than that within the grain. Smaller grain boundary results in reduced defect density. These defects frequently serve as charge trap centers so the optical bandgap energies tend to decrease.[35,36]

The electrical properties of the nickel oxide thin films, including Hall mobility (μ_H), carrier concentration (n_H), and resistivity (ρ), under various oxygen flow conditions, are presented in Fig. 5 and Table 2. The resistivity values are 0.65, 0.44, 0.28 and 0.43 Ω cm, corresponding to oxygen percentages of 20%, 25%, 30%, and 35%, respectively. The carrier mobility increases gradually from 0.43 $cm^2\ V^{-1}\ s^{-1}$ to 0.61 $cm^2\ V^{-1}\ s^{-1}$, when the oxygen level increases from 20% to 30% and then decreases to 0.20 $cm^2\ V^{-1}\ s^{-1}$ at an oxygen ratio of 35%. The carrier concentration increases from 2.23×10^{19} cm^{-3} to 7.46×10^{19} cm^{-3}. These values are considerably higher than those reported in a previous study.[37] This can be attributed to the

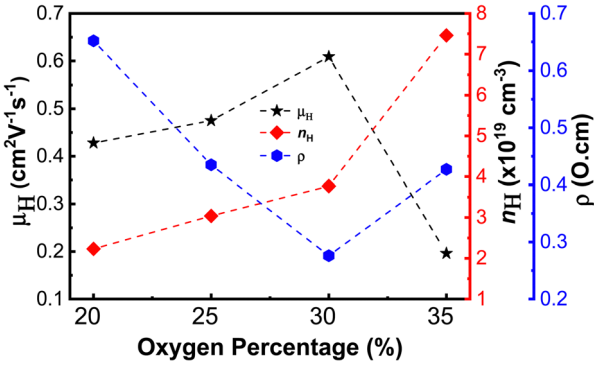

Fig. 5 The Hall mobility (μ_H), carrier concentration (n_H), and resistivity (ρ) *versus* the function of oxygen percentage of nickel oxide thin films.

Table 2 Optical and electrical properties parameters of nickel oxide thin films

	Optical properties		Electrical properties		
Sample	Transmittance (400–800 nm) (%)	E_g (eV)	Mobility ($cm^2\ V^{-1}\ s^{-1}$)	Carrier concentration ($\times 10^{19}$ cm^{-3})	Resistivity (Ω cm)
N-20	56	3.28	0.43	2.23	0.65
N-25	52	3.35	0.48	3.04	0.44
N-30	51	3.46	0.61	3.77	0.28
N-35	50	3.40	0.20	7.46	0.43

oxidation of one Ni^{2+} ion into two Ni^{3+} ions and a Ni vacancy in an oxygen-rich environment. The higher the oxygen inlet is, the more Ni^{3+} ions and free carriers are generated. This oxidation helps to maintain the electroneutral state of the nickel oxide thin film, as described in eqn (2).[28] However, for sample N-35, a great amount of defects reduce hole mobility due to defect scattering, leading to an increase in the resistivity of the film.

$$Ni^{2+} + \frac{1}{2}O_2 \rightarrow 2Ni^{3+} + O^{2-} + Ni_{vacancy} \quad (2)$$

The current density–voltage (J–V) characteristics of the p–n heterojunctions between the n-Si substrate and nickel oxide (oxygen ratios of 20% and 30%) are shown in Fig. 6. The nickel oxide thin film has successfully established a p–n heterojunction on the n-type Si substrate, as evidenced by the typical characteristic diode curves obtained. The J–V curves can be characterized using the thermoionic emission model shown in the following equation:[38,39]

$$J = J_0 \cdot \exp\left(\frac{qV}{nk_BT} - 1\right) \quad (3)$$

where J_0 is the saturation current density, q is the charge (1.6×10^{-19} C), T is the environmental temperature in K, k is the Boltzmann constant (J K^{-1}), and n is the ideality factor. In addition, J_0 can be expressed as:

$$J_0 = AA^*T^2 \exp\left(\frac{-q\phi_B}{k_BT}\right) \quad (4)$$

A is the contact area, A^* ($\sim$112 A K^{-2} cm^{-2} for n-Si) is the

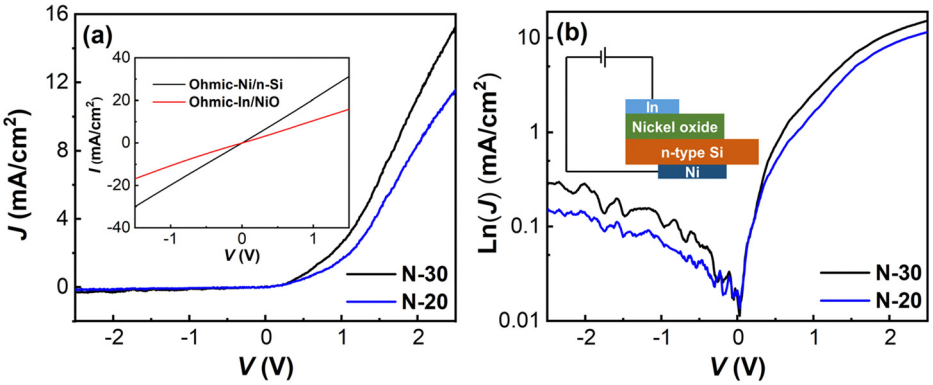

Fig. 6 Linear (a) and semi-logarithmic (b) J–V characteristics of the nickel oxide/n-Si diode. Inset of (a): I–V characteristics of Ni/n-Si and In/NiO.

Table 3 Characteristic parameters of the nickel oxide/n-Si heterojunction diode

Sample	$V_{\text{turn-on}}$ (V)	Ideality factor – n	Effective barrier heights – Φ_B (eV)	Rectification ratio (±2 V)	R_S (Ω)	Saturation current density (A cm^{-2})
N-20	0.91	9.62	0.71	64	230.79	1.66×10^{-6}
N-30	0.78	6.86	0.72	68	150.99	1.12×10^{-6}

Richardson constant and Φ_B is the barrier potential. Using these eqn (3) and (4), the ideality factor n can be determined from equation:

$$\frac{1}{n} = \frac{k_B T}{q} \cdot \frac{\mathrm{d} \ln J}{\mathrm{d} V} \quad (5)$$

For the N-20, and N-30 samples, the ideality factor values are 9.62, and 6.86, respectively. The corresponding effective barrier heights are 0.71 and 0.72 eV. The turn-on voltages ($V_{\text{turn-on}}$) of the diodes are 0.91 V and 0.78 V. Both the ideality factor and the series resistor (R_S) decrease with increasing oxygen flow. The electrical properties of nickel oxide films are obviously impacted by the additional oxygen inlet. The ideality factor of silicon diodes varies between 1 and 2, according to the Sah–Noyce–Shockley theory.[40] In diode applications, the value of n can exceed 2 as a result of the formation of multi-level recombination channels caused by a greater amount of defects at the interface between the nickel oxide and silicon materials.[38,41] Furthermore, the structural characteristics and the work function difference of the two layers are the key factors that determine the effective barrier height (Table 3).[38]

4. Conclusion

In summary, nickel oxide films were successfully reactively sputter deposited on glass and silicon substrates. When the partial oxygen ratio increases from 20% to 35%, analysis results indicate a phase transition from NiO to Ni_2O_3 corresponding to the transition of Ni^{2+} to Ni^{3+}, an increase in the Ni vacancy sites and enhancement of the hole concentration. As Ni vacancy density increased, the crystal size of the film decreased. This led to reduced carrier mobility and decreased film transmittance. The results show that at a 30% oxygen ratio, the nickel oxide thin films present the best electrical and optical properties with a transmittance of 51%, a bandgap energy of 3.46 eV, a carrier concentration of 3.77×10^{19} cm^{-3}, a mobility of 0.61 cm^2 V^{-1} s^{-1}, and a resistivity of 0.28 Ω cm. In addition, the I–V curves of Ni_2O_3/n-Si heterojunctions demonstrated that the best diode parameters (V_{OC} = 0.78 V, n = 6.86, and Φ_B = 0.72 eV) can be achieved at an oxygen percentage of 30%. The results demonstrate the potential of nickel oxide films for future electronic applications such as wide bandgap photodiodes.

Data availability

The data used to support the findings of this study are available from the corresponding author upon request.

Conflicts of interest

The authors have no conflicts to disclose.

Acknowledgements

This work belongs to the project T2025 funded by Ho Chi Minh City University of Technology and Education, Ho Chi Minh City, Vietnam.

References

1 C. Mrabet, M. Ben Amor, A. Boukhachem, M. Amlouk and T. Manoubi, *Ceram. Int.*, 2016, **42**, 5963–5978.
2 Y. Gong, S. Zhang, H. Gao, Z. Ma, S. Hu and Z. Tan, *Sustainable Energy Fuels*, 2020, **4**, 4415–4458.
3 B. G. S. González, G. Vescio, J. L. Frieiro, J. López-Vidrier, S. Hernández and A. Cirera, *Adv. Mater. Interfaces*, 2023, **10**, 2300035.

4 M. Mishra, S. Barthwal, B. R. Tak and R. Singh, *Phys. Status Solidi A*, 2021, **218**, 2100241.
5 J. D. Hwang and M. C. Lin, *Sens. Actuators, A*, 2023, **349**, 114087.
6 M. G. G. C. S. Chou, C. M. Hsiung, C. P. Wang and R. Y. Yang, *Int. J. Photoenergy*, 2010, **2010**, 9.
7 M. Matsumiya, F. Qiu, W. Shin, N. Izu, N. Murayama and S. Kanzaki, *Thin Solid Films*, 2002, **419**, 213–217.
8 W. L. Jang, Y. M. Lu, W. S. Hwang, T. L. Hsiung and H. P. Wang, *Appl. Phys. Lett.*, 2009, **94**, 10–13.
9 P. Salunkhe, M. A. Muhammed and D. Kekuda, *Appl. Phys. A: Mater. Sci. Process.*, 2021, **127**, 1–12.
10 K. Jouini, A. Raouafi, W. Dridi, M. Daoudi, B. Mustapha, R. Chtourou and F. Hosni, *Optik*, 2019, **195**, 163109.
11 F. A. F. Lahiji, S. Bairagi, R. Magnusson, M. A. Sortica, D. Primetzhofer, E. Ekström, B. Paul, A. le Febvrier and P. Eklund, *J. Vac. Sci. Technol., A*, 2023, **41**, 063402.
12 S. Nandy, U. N. Maiti, C. K. Ghosh and K. K. Chattopadhyay, *J. Phys.: Condens. Matter*, 2009, **21**, 115804.
13 M. C. Li, M. J. Dai, S. S. Lin, S. C. Chen, J. Xu, X. L. Liu, E. H. Wu, A. N. Ding, J. H. Gong and H. Sun, *Ceram. Int.*, 2022, **48**, 2820–2825.
14 H. Wu, L. Wang, Y. Wang, S. Guo and Z. Shen, *J. Alloys Compd.*, 2012, **525**, 82–86.
15 N. M. Vuong, T. N. Trung, T. T. Hien, N. D. Chinh, N. D. Quang, D. Lee, D. Kim, T. L. Phan and D. Kim, *Mater. Trans.*, 2015, **56**, 1354–1357.
16 N. K. Binh, P. N. Y. Nhi, T. B. Quan, P. M. Tam, N. N. Phuong, D. M. Tuan, P. T. K. Hang and P. H. Phuong, *J. Vac. Sci. Technol., B*, 2024, **42**, 062205.
17 H. D. Ngo, V. D. T. Truong, V. Q. Le, H. P. Pham and T. K. H. Pham, *Beilstein J. Nanotechnol.*, 2024, **15**, 253–1259.
18 M. S. Jamal, S. A. Shahahmadi, P. Chelvanathan, H. F. Alharbi, M. R. Karim, M. Ahmad Dar, M. Luqman, N. H. Alharthi, Y. S. Al-Harthi, M. Aminuzzaman, N. Asim, K. Sopian, S. K. Tiong, N. Amin and M. Akhtaruzzaman, *Results Phys.*, 2019, **14**, 102360.
19 H. L. Chen, Y. M. Lu and W. S. Hwang, *Mater. Trans.*, 2005, **46**, 872–879.
20 M. Aftab, M. Z. Butt, D. Ali, M. U. Tanveer and A. Hussnain, *Proc. Pakistan Acad. Sci. Part A*, 2020, **57**, 51–74.
21 P. Gao, L. J. Meng, M. P. Dos Santos, V. Teixeira and M. Andritschky, *Vacuum*, 2000, **56**, 143–148.
22 G. Gottardi, N. Laidani, V. Micheli, R. Bartali and M. Anderle, *Surf. Coat. Technol.*, 2008, **202**, 2332–2337.
23 A. H. Hammad, M. S. Abdel-wahab, S. Vattamkandathil and A. R. Ansari, *Phys. B*, 2019, **568**, 6–12.
24 S. Uhlenbrock, C. Scharfschwerdt, M. Neumann, G. Illing and H. J. Freund, *J. Phys.: Condens. Matter*, 1992, **4**, 7973–7978.
25 K. Xu, L. Wang, C. Ge, L. Wang, B. Wang, Z. Wang, C. Zhang and G. Liu, *Energy Environ. Mater.*, 2024, **7**, 1–11.
26 B. Sasi and K. G. Gopchandran, *Nanotechnology*, 2007, **18**, 115613.
27 A. M. Elseman, L. Luo and Q. L. Song, *Dalton Trans.*, 2020, **49**, 14243–14250.
28 H. Kim, K. Kim and J. Hong, *Coatings*, 2023, **13**, 1954.
29 S. Nandy, B. Saha, M. K. Mitra and K. K. Chattopadhyay, *J. Mater. Sci.*, 2007, **42**, 5766–5772.
30 H. Liu, W. Zheng, X. Yan and B. Feng, *J. Alloys Compd.*, 2008, **462**, 356–361.
31 A. H. Hammad, M. S. Abdel-wahab, S. Vattamkandathil and A. R. Ansari, *Phys. B*, 2019, **568**, 6–12.
32 F. Şenaslan, M. Taşdemir and A. Çelik, *Appl. Phys. A: Mater. Sci. Process.*, 2021, **127**, 1–9.
33 F. G. El Desouky, H. A. Saleh and D. Atta, *Phys. Scr.*, 2024, **99**, 75905.
34 Z. M. Gibbs, A. Lalonde and G. J. Snyder, *New J. Phys.*, 2013, **15**, 075020.
35 M. Kumar, *Mater. Res. Express*, 2019, **6**, 096404.
36 A. M. Reddy, C. W. Byun, S. K. Joo, A. S. Reddy and P. S. Reddy, *Electron. Mater. Lett.*, 2014, **10**, 887–892.
37 P. Salunkhe, A. V. Muhammed Ali and D. Kekuda, *Mater. Res. Express*, 2020, **7**, 016427.
38 S. Kaya, *Appl. Phys. A: Mater. Sci. Process.*, 2020, **126**, 1–9.
39 H. P. Pham, T. H. Y. Nguyen, A. H.-T. Nguyen, N. T. Vo, T. G. Le Thuy, H. H. Nguyen, H. T. M. Hoa and Q. T. Tran, *J. Photochem. Photobiol. A Chem.*, 2019, **388**, 112157.
40 J. M. Shah, Y. L. Li, T. Gessmann and E. F. Schubert, *J. Appl. Phys.*, 2003, **94**, 2627–2630.
41 M. Yilmaz, H. Kacus, M. L. Grilli and S. Aydogan, *J. Sandwich Struct. Mater.*, 2021, **23**, 1383–1402.